ChemPubSoc Europe

DOI: 10.1002/open.201800247

Open Access ChemistryOPEN Communications

Efficiency of 3D-Ordered Macroporous $La_{0.6}Sr_{0.4}Co_{0.2}Fe_{0.8}O_3$ as an Electrocatalyst for Aprotic Li-O_2 Batteries

Junfang Cheng,[a, b] Yuexing Jiang,[a] Lu Zou,[a] Ming Zhang,[c] Guozhu Zhang,[d] Ziling Wang,[a] Yizhen Huang,[a] Bo Chi,*[a] Jian Pu,[a] and Li Jian[a]

Li-O_2 batteries (LOBs) with an extremely high theoretical energy density have been reported to be the most promising candidates for future electric storage systems. Porous catalysts can be beneficial for LOBs. Herein, 3D-ordered macroporous $La_{0.6}Sr_{0.4}Co_{0.2}Fe_{0.8}O_3$ perovskite oxides (3D-LSCF) are applied as cathode catalysts in LOBs. With a high Brunauer-Emmett-Teller surface area (21.8 $m^2 g^{-1}$) and unique honeycomb-like macroporous structure, the 3D-LSCF catalysts possess a much higher efficiency than $La_{0.6}Sr_{0.4}Co_{0.2}Fe_{0.8}O_3$ (LSCF) nanoparticles. The unique 3D-ordered macropores play a significant role in the product deposition as well as oxygen and electrolyte transmission, which are crucial for the discharge-charge processes of LOBs.

As a possible alternative to state-of-the-art lithium-ion batteries, LOBs are currently attracted worldwide attention because of their extremely high theoretical energy density.[1–3] Unfortunately, many unsolved scientific challenges inhibit the practical applications, such as high overpotential, poor rate capacity and short cycle life, which are mainly due to the sluggish dynamics of oxygen reduction reaction ($2Li^+ + O_2 + 2e^- \rightarrow Li_2O_2$, ORR) and oxygen evolution reaction ($Li_2O_2 \rightarrow 2Li^+ + O_2 + 2e^-$, OER).[4] Therefore, to develop a bi-functional catalyst is highly desirable to accelerate the development of LOBs. These catalysts mainly include carbon materials, noble metals, nitrogen-containing metal compounds and transitional metal oxides.[5] Though noble metals may possess the highest bi-functional (ORR and OER) catalytic activities, the expensive prices prevent them from large-scale applications.[6]

As a member of transitional metal oxides, perovskites oxides have been reported as efficient catalysts in metal air batteries for their low price and excellent catalytic activity.[7–9] Besides, porous catalysts have been demonstrated to be advantageous in LOBs because of their facile pathway for oxygen and electrolyte diffusion together with more active sites during the ORR and OER processes.[10,11] However, the phase formation temperatures of perovskite oxides are often approaching or exceeding 800 °C, which could destroy the porous structure and damage the catalytic activity.[12,13] Therefore, it has great significance to prepare porous perovskite catalysts at lower temperature.

Herein, 3D-ordered macroporous $La_{0.6}Sr_{0.4}Co_{0.2}Fe_{0.8}O_3$ (3D-LSCF) perovskite oxide has been obtained through polystyrene sphere (PS) template removing method as the substitution of traditional sol-gel method in our previous work. The prepared 3D-LSCF and traditional LSCF are both applied as cathode catalysts in LOBs. The performance comparison indicates that the 3D-ordered macroporous structure is of vital importance for the performance enhancement of LOBs.

It can be seen that the particles of PSs are very uniform and the sizes are all around 400 nm (see Figure S1a). After centrifugation treatment, the monodispersed PSs are close-packed into colloidal crystal and form orderly arranged templates (see Figure S1b).

The X-ray diffraction (XRD) patterns of the precursors after being calcined in three different temperatures are presented in Figure 1. The peak intensity becomes stronger as the temperature increases. The diffraction peaks of the samples calcined in 600 °C and 650 °C are assigned to orthorhombic perovskite LSCF (JCPDS 89-1268). The impure phase $LaCo_{0.4}Fe_{0.6}O_3$ appears only in the temperature of 550 °C. Thus 600 °C can be the suitable calcination temperature to obtain pure LSCF without other phases.

The SEM image of the precursor calcined in 600 °C is shown in Figure 2a. After removing the orderly arranged PS templates, the positions of PSs form "air spheres" and the residual LSCF exhibited interconnected inorganic walls in three dimensions. The pore size of these connected walls is about 300 nm, which is smaller than that of PSs (400 nm). This is resulted from the shrink process during the calcination. For comparison, the LSCF nanoparticles via traditional sol-gel method is also obtained,

[a] Dr. J. Cheng, Dr. Y. Jiang, Dr. L. Zou, Dr. Z. Wang, Dr. Y. Huang, Prof. B. Chi, Prof. J. Pu, Prof. L. Jian
Center for Fuel Cell Innovation
Huazhong University of Science and Technology
Wuhan 430074, China
E-mail: chibo@hust.edu.cn
[b] Dr. J. Cheng
International Institute for Carbon-Neutral Energy Research
(WPI-I2CNER), Kyushu University
744 Moto-oka, Nishi-ku Fukuoka, 819-0395, Japan
[c] Dr. M. Zhang
Fujian Institute of Research on the Structure of Matter
Chinese Academy of Sciences
Fuzhou 350002, China
[d] Dr. G. Zhang
Institute for Materials Chemistry and Engineering
Kyushu University
6-1 Kasuga-Koen, Kasuga, Fukuoka 816-8580, Japan

Supporting information for this article is available on the WWW under https://doi.org/10.1002/open.201800247

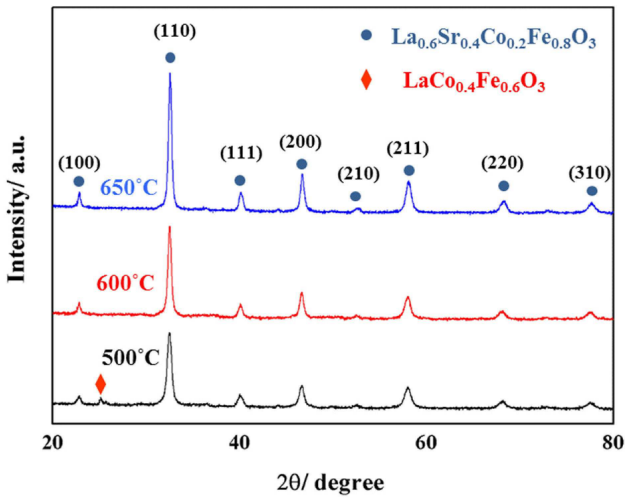

Figure 1. X-ray diffraction patterns of precursors calcined at different temperatures.

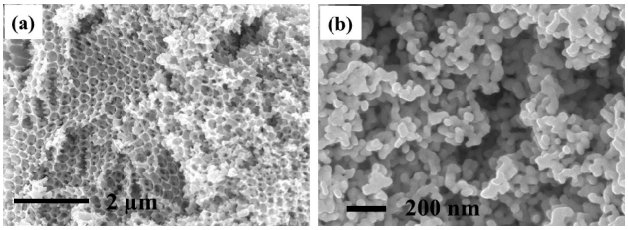

Figure 2. SEM image of a) the 3D-LSCF after calcined in 600 °C and b) the LSCF prepared by sol-gel method.

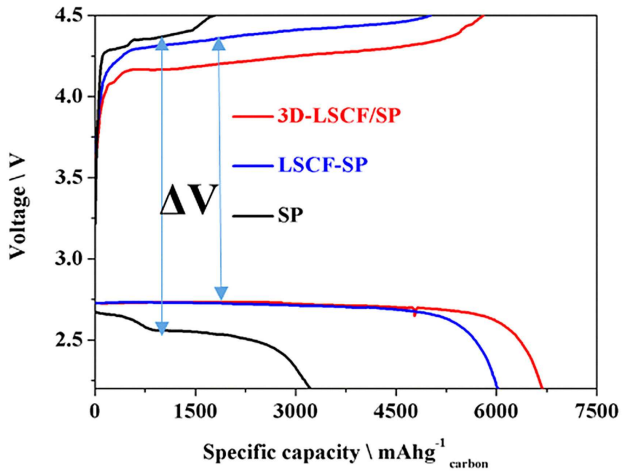

Figure 3. Full discharge-charge curves of LOBs with different cathodes at current density of 400 mA g^{-1}.

Table 1. Discharge–charge capacities and coulombic efficiencies of LOBs with different cathodes at current density of 400 mA g^{-1}.

Cathode	Discharge capacity [mAh g^{-1}]	Charge capacity [mAh g^{-1}]	Coulombic efficiency [%]
SP	3217	1787	55.55
LSCF-SP	6027	5013	83.17
3D-LSCF/SP	6693	5807	86.76

which are shown in Figure 2b. The particle size of LSCF is about 50 nm and there are no connected pores between these particles. Generally, the open and interconnected 3D-ordered macroporous structure can exhibit higher specific area and provide more surface sites. The BET surface area is also obtained and the values of 3D-LSCF and LSCF are 21.8 $m^2 g^{-1}$ and 10.69 $m^2 g^{-1}$ respectively.

The full discharge-charge performance of LOBs with these two catalysts is further examined. For comparison, the rate performance of LOBs with pure SP cathode is also conducted, as shown in Figure 3. At current density of 400 mA g^{-1}, the specific discharge capacity of SP cathode is only 3217 mAh g^{-1}. When used LSCF and 3D-LSCF catalysts, the discharge performances have been increased to 6027 mAh g^{-1} and 6693 mAh g^{-1}. The detail comparison is presented in Table 1. More obvious enhancement lies in charge capacity. Without catalyst, the charge capacity of LOBs is just 1787 mAh g^{-1}. However, the charge capacities of LOBs with LSCF-SP cathode and 3D-LSCF/SP cathode are advanced to 5013 mAh g^{-1} and 5807 mAh g^{-1}. The charge-discharge voltage difference (ΔV) can be used to measure the overpotential, which can be dramatically reduced by the two catalysts especially for 3D-LSCF.

The value of coulombic efficiency is defined by charge capacity/discharge capacity, as shown in Table 1. The absence of LSCF and 3D-LSCF catalysts make the coulombic efficiency of LOBs dramatically raise to 83.17% and 86.76% from 55.55%. The aggregation of products during the discharge process can cause high charge voltage and then terminate the charge process immediately. And this is the reason for the low capacity and coulombic efficiency of LOBs with pure SP cathode. However, with the assistance of LSCF catalyst, the morphology of the discharge products will change into different shape which will cause lower overpotential. During the following charge process, LSCF catalyst can also accelerate the decomposition of products, resulting in lower charge voltage and higher capacity. Furthermore, 3D-LSCF catalyst with higher BET surface area and 3D-ordered macroporous structure would certainly ensure the high availability of catalytic active sites and thus contribute to much lower overpotential and more obvious capacity enhancement.[14,15]

Cycle stability is also very crucial to evaluate the performance of LOBs. At current density of 400 mA g^{-1}, LOBs with pure SP cathode can run about 58 cycles (see Figure S2). LOBs show minimal attenuation at the first 30 cycles and the later attenuation is attributed to the progressively higher overpotential.

With the catalytic effect of LSCF, the cycle number of LOBs has increased to above 150 (Figure 4a). The performance of LOBs with LSCF-SP cathode is very stable at the beginning 90 cycles. During the following cycles, the products accumulated gradually on the surface of electrode, thus weaken the cycle performance and the LOBs end up at about the 156th cycle. The introduction of 3D-LSCF catalyst can further improve

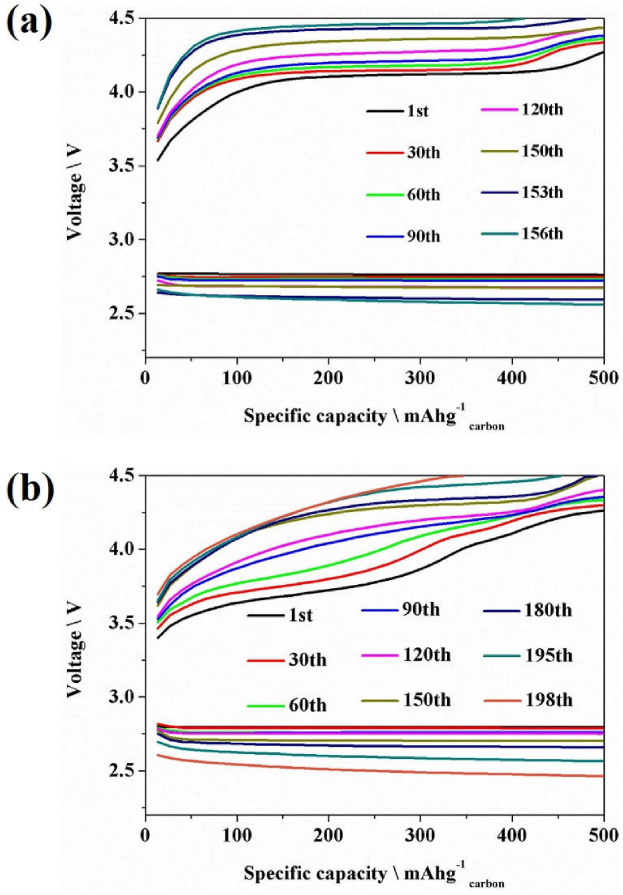

Figure 4. Cycle performances of LOBs with a) LSCF-SP and b) 3D-LSCF/SP cathodes at current density of 400 mA g^{-1}.

the cycle stability. The LOBs with 3D-LSCF/SP cathode can run for approximately 150 cycles (Figure 4b) without obvious degradation, and then gradually deteriorates as the cycle time increases. For comparison, herein the cycle performance of LOBs with some other perovskite catalysts are presented. For example, with a limited capacity of 500 mAh g^{-1}, LOBs with $La_{0.6}Sr_{0.4}Co_{0.9}Mn_{0.1}O_3$, $La_{0.6}Sr_{0.4}CoO_{3-6}$, $La_{0.8}Sr_{0.2}Mn_{0.6}Ni_{0.4}O_3$ nanoparticles and hierarchical mesoporous/macroporous $La_{0.5}Sr_{0.5}CoO_{3-6}$ nanotubes catalysts can run 53 cycles at 100 mA g^{-1}, 51 cycles at 0.1 mA cm^{-1}, 79 cycles at 200 mA g^{-1} and 50 cycles at 0.1 mA cm^{-1}, respectively. So the cycle stability of LOBs with 3D-LSCF catalyst is very outstanding among other perovskite catalysts.[8,16,17]

The overpotential can also be seen from the cycle curves and show the notable trend of 3D-LSCF/SP < LSCF-SP < SP. For all cathodes, the discharge plateaus are stable with only one stair. However, it is worth noting that the charge plateaus exhibit two stairs for 3D-LSCF/SP cathode at the beginning cycles while one stair for SP and LSCF-SP cathode during all cycle times. The two stairs with different ΔV is related with the unique microstructure of 3D-LSCF catalyst. The honeycomb-like "air spheres" can provide sufficient void volume for products deposition and more abundant oxygen and electrolyte transportation paths, resulting in lower charge voltage at the beginning charge stage. The second stair comes from the later deposition of products. As the residual products accumulate cycle by cycle, the charge voltage ascends and then evolves into one stair in the subsequent cycles. Even the charge voltage has risen later, it is still lower than LOBs with other two cathodes. The single charge stair in the full discharge-charge curves (Figure 3) may be due to the excessive accumulation of discharge products in the full discharge process. 3D-LSCF with high BET surface area and unique "air spheres" can provide more sufficient space for products deposition and more catalytic active sites, as well as more oxygen and electrolyte transmission channels to facilitate the formation and decomposition of products, and then cause lower overpotential, resulting in better rate performance and cycle stability.[18,19]

Experimental Section

Before preparing 3D-LSCF, the PS templates should be obtained. The monodispersed polystyrene spheres were synthesized by emulsion polymerization. Sodium dodecyl sulfate (SDS) and potassium persulfate (KPS) were dissolved in the mixture solution of ethanol and water. Then styrene (CP) was added to the solution before stirring in 65 °C under N_2 atmosphere for 6 h. After centrifugation at 2000 rpm for 20 h, the close-packed PS templates were obtained after vacuum drying overnight.[20] Stoichiometric amounts of relevant metal nitrates ($La(NO_3)_2 \cdot 6H_2O$:$Sr(NO_3)_2$:$Co(NO_3)_2 \cdot 6H_2O$:$Fe(NO_3)_3 \cdot 9H_2O$ = 6:4:2:8) were dissolved in an ethylene glycol (EG) -methanol (30–50 vol%) mixed solvent to form precursor solution. The prepared PS templates were infiltrated in the precursor solution for 1 h and then filtrated to remove the excess solution. After drying in 60 °C for 2 h, the PS templates were removed in flowing air at 350 °C. Then the obtained samples are heated in different temperatures to form perovskite phase.[21] The traditional perovskite $La_{0.6}Sr_{0.4}Co_{0.2}Fe_{0.8}O_3$ (LSCF) nanoparticles were synthesized by sol-gel method in our previous reports.[22]

The LOBs used Swagelok-type test mold and were assembled layer by layer with lithium ribbon (China Energy Lithium Co., LTD., ϕ 15.6 mm × 0.4 mm) as anode, glass fiber (Whatman) as separator, 1 M lithium trifluoromethanesulfonate (LiTFSI) in dimethylsulfoxide (DMSO) as electrolyte and the air cathode. All the processes were conducted in an argon-filled glove box with oxygen and moisture less than 1 ppm. The air cathode was prepared by screen printing the mixed slurry (cathode materials) onto the carbon paper (ϕ 15.6 mm × 1.7 mm, Tory). The mixed slurry is composed of Super P (SP), as-prepared catalysts (3D-LSCF or LSCF), polyvinylidene fluoride (PVDF) (Sigma Aldrich, MW 534,000, 99.9%) binder in a mass ratio of 60:30:10. For comparison, the cathode without catalyst was also prepared and the mass ratio of SP and PVDF was 90:10. The electrodes with or without catalyst were labeled as 3D-LSCF/SP, LSCF-SP and SP cathode. The loading of pure SP electrode (SP + PVDF) onto the disks was about 2.2 ± 0.2 mg and the loading of LSCF-SP electrode (SP + LSCF + PVDF) onto the disks was about 3.2 ± 0.2 mg.

The phase structures of catalysts were analyzed by X'Pert PRO X-ray diffractometer with CuK_α radiation. The morphology was investigated by field emission scanning electron microscopy (FE-SEM, FEI, Sirion 200). The specific surface area of the oxides was determined by using the Brunauer-Emmett-Teller (BET) method. The electrochemical performances of the batteries were evaluated in a Hantest cycler (Wuhan Hantest Technology Co., Ltd.) at room temperature and the discharge-charge voltages were recorded within a potential range of 2.2 ~ 4.5 V under O_2 atmosphere. Before

test, the batteries were rested for 5 h to reach equilibrium of the oxygen concentrations and moisture of the electrolyte. The rate and cycle performance were tested at current density of 400 mA g^{-1}.

Acknowledgements

The authors would like to thank Materials Characterization Center of Huazhong University of Science and Technology for samples characterization assistance and the Innovation Foundation of Graduate Innovation and Entrepreneurship Base of HUST (No. 2015650011) for financial support.

Conflict of interest

The authors declare no conflict of interest.

Keywords: Li-O_2 batteries · perovskite phases · nanostructures · overpotential · catalytic efficiency

[1] M. Armand, J.-M. Tarascon, *Nature* **2008**, *451*, 652–657.
[2] P. G. Bruce, S. A. Freunberger, L. J. Hardwick, J.-M. Tarascon, *Nat. Mater.* **2012**, *11*, 19–29.
[3] Y. Jiang, J. Cheng, L. Zou, X. Li, Y. Gong, B. Chi, *Electrochim. Acta* **2016**, *210*, 712–719.
[4] L. Grande, E. Paillard, J. Hassoun, J.-B. Park, Y.-J. Lee, Y.-K. Sun, S. Passerini, B. Scrosati, *Adv. Mater.* **2015**, *27*, 784–800.
[5] Z.-L. Wang, D. Xu, J.-J. Xu, X.-B. -Zhang, *Chem. Soc. Rev.* **2014**, *43*, 7746–7786.
[6] H.-G. Jung, Y. S. Jeong, J.-B. Park, Y.-K. Sun, B. Scrosati, Y. J. Lee, *ACS Nano* **2013**, *7*, 3532–3539.
[7] M. Yuasa, T. Matsuyoshi, T. Kida, K. Shimanoe, *J. Power Sources* **2013**, *242*, 216–221.
[8] N. Sun, H. Liu, Z. Yu, Z. Zheng, C. Shao, *Solid State Ionics* **2014**, *268*, 125–130.
[9] W. Yang, J. Salim, S. Li, C. Sun, L. Chen, J. B. Goodenough, Y. Kim, *J. Mater. Chem.* **2012**, *22*, 18902–18907.
[10] A. Vignesh, M. Prabu, S. Shanmugam, *ACS Appl. Mater. Interfaces* **2016**, *8*, 6019–6031.
[11] J. J. Xu, D. Xu, Z. L. Wang, H. G. Wang, L. L. Zhang, X. B. Zhang, *Angew. Chem. Int. Ed.* **2013**, *52*, 3887–3890; *Angew. Chem.* **2013**, *125*, 3979–3982.
[12] Q. Xu, S. Song, Y. Zhang, Y. Wang, J. Zhang, Y. Ruan, M. Han, *Electrochim. Acta* **2016**, *191*, 577–585.
[13] J. Chen, F. Liang, L. Liu, S. Jiang, B. Chi, J. Pu, J. Li, *J. Power Sources* **2008**, *183*, 586–589.
[14] R. Black, J.-H. Lee, B. Adams, C. A. Mims, L. F. Nazar, *Angew. Chem.* **2013**, *125*, 410–414; *Angew. Chem. Int. Ed.* **2013**, *52*, 392–396.
[15] J. Cheng, Y. Jiang, M. Zhang, L. Zou, Y. Huang, Z. Wang, B. Chi, J. Pu, J. Li, *Phys. Chem. Chem. Phys.* **2017**, *19*, 10227–10230
[16] Z. Ma, X. Yuan, L. Li, Z.-F. Ma, *Chem. Commun.* **2014**, *50*, 14855–14858.
[17] Z. Chang, J. Xu, X. Zhang, *Adv. Energy Mater.* **2017**, *7*, 1700875.
[18] D. Zhai, H.-H. Wang, J. Yang, K. C. Lau, K. Li, K. Amine, L. A. Curtiss, *J. Am. Chem. Soc.* **2013**, *135*, 15364–15372.
[19] P. Tan, W. Shyy, T. S. Zhao, Z. H. Wei, L. An, *J. Power Sources* **2015**, *27*, 8133–140.
[20] B. Y. Xia, B. Gates, Y. Yin, Y. Lu, *Adv. Mater.* **2000**, *12*, 693–713.
[21] J.-J. Xu, Z.-L. Wang, D. Xu, F.-Z. Meng, X.-B. Zhang, *Energy Environ. Sci.* **2014**, *7*, 2213–2219.
[22] J. Cheng, M. Zhang, Y. Jiang, L. Zou, Y. Gong, B. Chi, J. Pu, J. Li, *Electrochim. Acta* **2016**, *191*, 106–115.

Manuscript received: November 9, 2018
Revised manuscript received: January 17, 2019